

Provided for non-commercial research and education use.
Not for reproduction, distribution or commercial use.

Volume 63, October 2012 ISSN 0010-938X



CORROSION SCIENCE

The Journal on Environmental Degradation of Materials and its Control
Editor-in-Chief: G. T. BURSTEIN, University of Cambridge, U.K.
An Official Journal of the Institute of Corrosion

CONTENTS

Letter G. E. GALLO and J. S. POPOVIC	1 Monitoring active corrosion of metals in natural environments with magnetometry
Papers Y.-I. CHOI, S. SALMAN, K. KURODA and M. OKIBO R. AUTEMGRUBER, G. LUCKENEDER and A. W. HÄSSL M. WANG, J. WANG, H. FENG and W. KU A. FRIGNANI, V. GRASSI, F. ZANOTTO and F. ZUCCHI M. BEHAZIN, M. C. BISSINGER, J. J. NOËL and J. C. WEIN J. K. PAIK and D. K. KIM M. TROUBA, S. P. TRASATTI and D. O. FIAMINI A. HOFAR, M. PALM, P. KRATOCHVIL, V. VOHRKOVA and S. DANIŠ L. LI, X. ZHANG, J. LI, J. HE, S. ZHANG and F. PAN J. XU, E.-H. HAN and X. WU G.-L. SONG and Z. XU V. SHANKAR RAO, J. LIM, I. S. HWANG and L. K. SINGHAI	5 Improvement in corrosion characteristics of AZ31 Mg alloy by square pulse anodizing between transpassive and active regions 12 Corrosion of pre-hardened galvanized steel 20 Effect of Ag ₃ Sn intermetallic compounds on corrosion of Sn-3.0Ag-0.5Cu solder under high-temperature and high-humidity condition 29 Inhibition of AZ31 Mg alloy corrosion by anionic surfactants 40 Comparative study of film formation on high-purity Co and Sulfite-6: Probing the roles of a chromium oxide layer and gamma-radiation 51 Advanced method for the development of an empirical model to predict time-dependent corrosion wastage 59 The effect of aluminium alloy secondary phases on amine-based silane protection capacity 71 High-temperature oxidation behaviour of Zr alloyed Fe ₃ Al-type iron aluminide 82 Adsorption and corrosion inhibition of <i>Omanthus fragran</i> leaves extract on carbon steel 91 Acoustic emission response of 304 stainless steel during constant load test in high temperature aqueous environment 100 Crystal orientation and electrochemical corrosion of polycrystalline Mg 113 Characterization of oxide scales grown on 216L stainless steels in liquid lead–bismuth eutectic

Contents continued on outside back cover
<http://www.elsevier.com/locate/corsci>

This article appeared in a journal published by Elsevier. The attached copy is furnished to the author for internal non-commercial research and education use, including for instruction at the authors institution and sharing with colleagues.

Other uses, including reproduction and distribution, or selling or licensing copies, or posting to personal, institutional or third party websites are prohibited.

In most cases authors are permitted to post their version of the article (e.g. in Word or Tex form) to their personal website or institutional repository. Authors requiring further information regarding Elsevier's archiving and manuscript policies are encouraged to visit:

<http://www.elsevier.com/copyright>



Contents lists available at SciVerse ScienceDirect

Corrosion Science

journal homepage: www.elsevier.com/locate/corsci

Comparative study of film formation on high-purity Co and Stellite-6: Probing the roles of a chromium oxide layer and gamma-radiation

M. Behazin^a, M.C. Biesinger^b, J.J. Noël^a, J.C. Wren^{a,*}

^aDepartment of Chemistry, Western University, 1151 Richmond Street, London, Ontario, Canada N6A 5B7

^bWestern University, Surface Science Western, 999 Collip Circle, London, Ontario, Canada N6G 0J3

ARTICLE INFO

Article history:

Received 15 August 2011

Accepted 17 May 2012

Available online 26 May 2012

Keywords:

- A. Alloy
- A. Cobalt
- B. Polarization
- B. EIS
- B. XPS
- C. Anodic films

ABSTRACT

Gamma-irradiation significantly increases the corrosion potential on pure Co and the cobalt alloy, Stellite-6. To understand the radiation-induced corrosion of these materials, electrochemical studies of film formation and conversion on these metals were performed as a function of potential under both potentiodynamic and potentiostatic conditions. The oxidized surfaces were characterized by electrochemical impedance spectroscopy and X-ray photoelectron spectroscopy. Four characteristic potential regions are identified for anodic oxidation. Comparison of the behavior of pure cobalt and a cobalt alloy provides an insight into the role of an initial air-formed chromium oxide layer on the oxidation of Stellite-6 under different corrosion conditions.

© 2012 Elsevier Ltd. All rights reserved.

1. Introduction

Stellite-6 is a Co-based alloy with a complex metallurgical structure. Due to its high mechanical strength and corrosion resistance, this alloy is used in places that require high wear resistance, such as valve facings and ball bearings. These properties make Stellite-6 a significant alloy choice in nuclear power reactors. However, in a reactor core stable ⁵⁹Co can absorb a neutron to become the radioactive isotope, ⁶⁰Co. Thus, one of the operational and safety issues related to the use of cobalt-containing materials in a nuclear reactor is the potential formation of radioactive ⁶⁰Co from ⁵⁹Co released into the reactor core by corrosion. The ⁶⁰Co created in this way constitutes a safety hazard for plant workers who have to perform maintenance on the reactor because the ⁶⁰Co deposits on coolant circuit surfaces outside the reactor core [1].

Although Stellite-6 is known to be highly corrosion resistant under normal water conditions [1–3], its corrosion behavior in the presence of ionizing radiation has not been well established. Corrosion kinetics in water depend on both the aqueous redox conditions and the physical and chemical nature of the alloy surface. The high radiation fields present in a reactor core will cause water to decompose into a range of redox-active species (both highly oxidizing (e.g., ·OH, H₂O₂) and highly reducing (e.g., ·e_{aq}⁻, ·O₂⁻). These species can significantly influence corrosion kinetics [4,5].

There are extensive corrosion studies reported for Co [6–12] and some Co-alloys [2,13,14]. However, there are fewer studies on Stellite-6 alloy in the literature [1,3]. Those corrosion studies have shown that a complex carbide network in the alloy matrix makes Stellite-6 resistant to wear, galling and corrosion, and that this resistance is retained at high temperatures (ca 300 °C) [1,3]. Systematic studies of Stellite-6 corrosion, and particularly in the presence of ionizing radiation are rare. The limited information on Stellite-6 corrosion mechanisms and kinetics as a function of aqueous conditions makes it difficult to assess the corrosion susceptibility of these alloys in the transient aqueous environments present in a reactor coolant system.

In this study, oxide formation and conversion on Stellite-6 in borate solution at pH 10.6 and room temperature were studied as a function of electrode potential under both potentiodynamic and potentiostatic conditions. The pH value is that maintained in the coolant water in CANDU[®] reactor coolant (pH measured at 25 °C) (a value chosen to minimize the corrosion of the carbon steel reactor components). It is an interesting choice for corrosion studies because the solubility of cobalt oxide species is at a minimum near this pH [11,15]. Consequently, oxide formation is preferred over metal dissolution during corrosion and, hence, oxide formation can be studied more easily. In support of our investigation of the corrosion behavior of Stellite-6, experiments on high purity cobalt were also carried out under the same conditions. Knowledge gained from the Co study aids in the interpretation of the anodic oxidation processes occurring on the Stellite-6 alloy. Various electrochemical methods, such as corrosion potential

* Corresponding author. Tel.: +1 519661 2111x86339; fax: +1 519 661 3022.
E-mail address: jcwren@uwo.ca (J.C. Wren).

(E_{CORR}) measurements, cyclic voltammetry, and electrochemical impedance spectroscopy (EIS) were used to study the corrosion kinetics, and the oxide films formed on the metals were further examined using scanning electron microscopy (SEM) and X-ray photoelectron spectroscopy (XPS).

2. Experimental

The two materials studied in this work are high-purity cobalt (99.95% purity and henceforth identified as Co) and Stellite-6 (Metals Samples Company). The alloy composition of Stellite-6 is presented in Table 1. Electrodes prepared from the metals had a flat, circular face, with a surface area of 10 mm² in the case of Stellite-6 and 12.5 mm² in the case of Co. Prior to each experiment the coupon surface was abraded manually with 400, 600, and then 1200 grit SiC papers, polished with 1 μm MetaDi Supreme diamond paste suspension (Buehler) on Texmet microcloth (Buehler), and then finally sonicated in an acetone/methanol mixture for 5 min to remove surface residues. The polished coupons were then sealed within multiple layers of polyolefin heat shrink tubing, leaving only the polished face exposed to the electrolyte solution. SEM images of as-prepared Co and Stellite-6 electrode surfaces are presented in Fig. 1. The Stellite-6 images show the presence of two distinct phases: a chromium-rich phase (dark areas) and a cobalt-rich phase (light areas).

2.1. Electrochemical cell

A three-electrode system consisting of a working electrode (the Co or Stellite-6 coupon), a reference electrode, and a counter electrode was used. A saturated calomel electrode (SCE, Fisher Scientific) was used as the reference electrode in all experiments except for the E_{CORR} measurements in the gamma-irradiation cell. The gamma irradiation experiments employed a Hg/HgO reference electrode (Radiometer Analytical) in a 1.0 M KOH solution because this electrode has been shown to be more radiation-resistant than SCE or Ag/AgCl electrodes [16]. The Hg/HgO electrode has a potential of -0.131 V versus SCE. All potential values in this paper are quoted against the SCE scale to facilitate comparisons with our other work and other data reported in the literature.

Table 1
Chemical composition of Stellite-6 (in wt.%).

W	Mn	Mo	Si	C	Ni	Fe	Cr	Co
0.27	0.27	0.41	1.07	1.43	2.62	2.92	27.62	Bal.

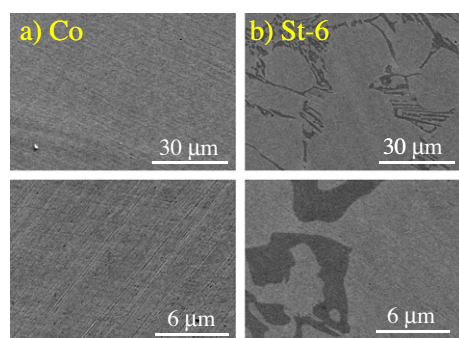


Fig. 1. SEM images of the surfaces of freshly prepared high-purity Co on the left hand panels and freshly prepared Stellite-6 on the right hand panels. Two magnification scales are used to show the degree of surface uniformity.

2.2. Solutions

All experiments were conducted at room temperature in Ar-sparged 0.01 M sodium borate solutions. The solutions were prepared using reagent grade Na₂B₄O₇ (Caledon Laboratories Ltd.) and water purified using a NANOpure Diamond UV ultra-pure water system (Barnstead International) with a resistivity of 18.2 M Ω cm. A pH of 10.6 was obtained by adding appropriate amounts of 1 M NaOH (Caledon Laboratories Ltd.) solution to the borate solution. The pH was measured prior to each experiment using an Accumet AB15 pH meter with standard size glass body combination electrode (Accumet 13-620-530).

2.3. Radiation source

All irradiation experiments were conducted in an MDS Nordion Gammacell 220 Excel Cobalt-60 irradiator. The electrochemical cell was positioned inside the gammacell sample chamber and the chamber was lowered into the irradiation zone, a cylindrical cavity surrounded by 11 tubular pencils containing ⁶⁰Co. The absorbed radiation dose rate in the cavity during the period of experimentation was 5.5 kGy h⁻¹, where 1 Gy is equivalent to 1 J of energy absorbed per kg of water.

2.4. Procedure

A Solartron model 1480 multistat and a Solartron model 1255 frequency response analyzer were used in all electrochemical measurements. Corrware™ and Zplot™ software (Scribner Associates) were used for experiment control, data acquisition and analysis. Electrochemical impedance spectroscopy (EIS) was performed by applying a sinusoidal potential stimulus of 10 mV amplitude on the DC bias potential used in the potentiostatic polarization, over a frequency range of 10⁻³ to 10⁴ Hz.

Before each experiment the electrolyte solution was Ar-purged for at least 30 min. The freshly prepared working electrode was then cathodically cleaned at $-1.1V_{\text{SCE}}$ for 5 min. For tests performed under each set of water conditions, a series of three electrochemical tests was performed on each material: (1) corrosion potential measurement, (2) cyclic voltammetry, and (3) potentiostatic polarization measurement. During the potentiostatic polarization tests, the current response was monitored as a function of time and EIS spectra were periodically recorded. At the end of each potentiostatic test, the electrode was removed from the cell, dried with Ar gas, and stored in a leak-tight vial. The electrode handling was performed in an Ar-purged glove box to minimize air oxidation and electrode contamination prior to surface analysis. Later the electrode was transferred in a sealed container and the electrode surface was analyzed by either SEM or XPS.

2.5. Surface analyses

An Hitachi S-4500 field emission SEM, operating in high-resolution mode, was used to examine the morphology of corrosion product deposits. X-ray photoelectron spectra were acquired on a KRATOS Axis Nova spectrometer using monochromatic Al K(alpha) radiation and operating at 210 W, with a base pressure of 10⁻⁸ Pa. Under normal analysis conditions, the analysis spot size was approximately 400 \times 700 μm . All spectra were calibrated with respect to the C 1s band (from adventitious carbon) whose energy was set to 284.8 eV [17]. Broad-spectrum survey scans were recorded at a pass energy of 160 eV to verify surface composition and cleanliness. High-resolution spectra (20 eV pass energy) were used to examine the Co 2p (binding energy, BE, at \sim 780 eV), Cr 2p (\sim 574 eV), O 1s (\sim 530 eV), and C 1s (\sim 285 eV) bands [17].

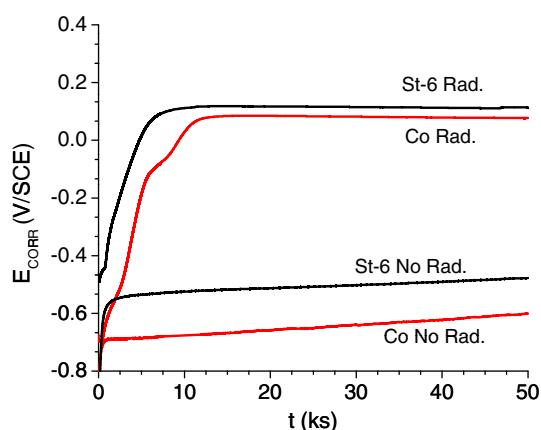


Fig. 2. E_{CORR} as a function of time recorded on Co and Stellite-6 electrodes in an Ar-purged borate solution at pH 10.6 and room temperature, in the presence and absence of gamma-irradiation (at an absorbed dose rate of 5.5 kGy h^{-1}).

3. Results and discussion

3.1. Corrosion potentials under gamma-irradiation

Fig. 2 shows the effect of gamma-irradiation on the E_{CORR} of the Co and Stellite-6 electrodes. In the absence of radiation, the E_{CORR} of both materials is established quickly (in ~ 20 min) and this value then trends very slowly and steadily upward, increasing from -0.7 V_{SCE} to -0.6 V_{SCE} over 50 h on the Co electrode and a similar increase is observed for Stellite-6, but with E_{CORR} about 0.12 V more positive. When the corroding system is exposed to gamma-radiation, E_{CORR} reaches different, higher values (increasing from -0.7 V_{SCE} to 0.08 V_{SCE} for Co and increasing from -0.48 V_{SCE} to 0.12 V_{SCE} for Stellite-6). It takes longer to reach the higher steady-state values ($\sim 1 \text{ h}$ for Stellite-6 and $\sim 3 \text{ h}$ for Co), but, once reached, the E_{CORR} values remained constant with time.

Corrosion of a metal in water involves oxidation of metal species coupled with reduction of aqueous species. This process depends on the electric field potential at the metal (or alloy) and water interface. When no external voltage is applied to the metal, the net rates of oxidation and reduction must be equal to maintain charge balance. The potential on the corroding surface at which this balance occurs is defined as the corrosion potential, E_{CORR} . The rate of metal oxidation depends on the potential difference between E_{CORR} and the equilibrium potential of the metal redox reaction. Since the corrosion potential is a function of both anodic and cathodic reaction rates, changes in aqueous redox environment as well as changes in the oxide film can change the corrosion potential. When exposed to ionizing radiation a small fraction of water decomposes to create a range of redox active species (gamma radiation absorbed directly by a metal coupon dissipates as heat). This is the reason for the changes in E_{CORR} seen in Fig. 2.

The impact of ionizing radiation on E_{CORR} for Co and Stellite-6 is consistent with the observations of this impact on other alloys. Gamma-irradiation has been shown to increase E_{CORR} from $-0.65 \pm 0.05 \text{ V}_{SCE}$ to $0.0 \pm 0.1 \text{ V}_{SCE}$ on carbon steel [18] and E_{CORR} from $-0.4 \pm 0.1 \text{ V}_{SCE}$ to $0.05 \pm 0.05 \text{ V}_{SCE}$ on stainless steel [19], at pH 10.6 and room temperature. Previous studies on carbon steel [16,18,20] have shown that gamma-irradiation affects the corrosion process primarily by producing redox active species (such as H_2O_2) in the aqueous phase.

Oxide formation and conversion on Co and Stellite-6 were investigated as a function of potential under potentiodynamic (using cyclic voltammetry) and potentiostatic conditions over a potential range that encompasses the E_{CORR} values observed in the absence and presence of radiation.

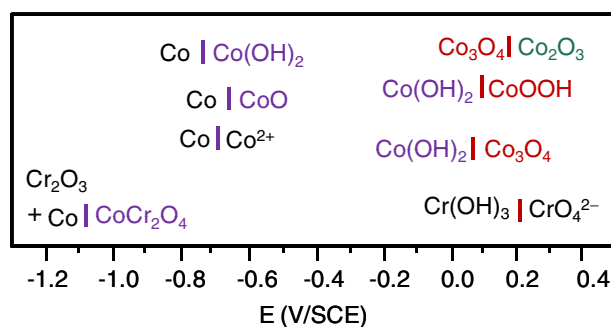


Fig. 3. Calculated equilibrium potentials for various redox reactions (at pH 10.6 and 25°C) are indicated by vertical lines.

3.2. Oxide formation and conversion under potentiodynamic conditions

3.2.1. Assignments of the current peaks in cyclic voltammograms

Cyclic voltammetry (CV) was performed to establish characteristic potential ranges for the oxides that can be formed on Co and Stellite-6 under potentiodynamic conditions. The growth rate of the oxide layer in each potential region, as defined in this CV study, was then investigated in detail under potentiostatic conditions, see Section 3.3. To aid in the assignment of the current peaks seen in the cyclic voltammograms, the thermodynamic equilibrium potentials (E^{eq}) for the redox reactions of cobalt and chromium species at pH 10.6 were calculated from reported standard potentials for the species [21]. These potentials are shown using vertical lines in Fig. 3. In addition to thermodynamic constraints, reaction kinetics can control oxide formation. Since the potential scan rate can alter the time available for a given reaction, differences observed in potentiodynamic and potentiostatic studies provide information on the role of kinetics on oxide formation. Although we acquired CVs as a function of a number of parameters (electrode rotation rate, potential scan rate and pH), only key results are present here.

3.2.1.1. High-purity Co. Cyclic voltammograms recorded on a Co electrode are shown in Fig. 4. The overlapping anodic peaks labeled A1 (-0.7 to -0.6 V_{SCE}) and A2 (-0.5 V_{SCE}) can both be attributed to the oxidation of Co–Co^{II} oxide/hydroxide ($\text{CoO}/\text{Co}(\text{OH})_2$). There are two pathways for the oxidation of Co–Co^{II}. Peak A1 lies below the E_{eq} for the oxidation of Co in the bulk metal to $\text{Co}(\text{OH})_2$ and is assigned to an oxidation process involving Co in a few surface monolayers:

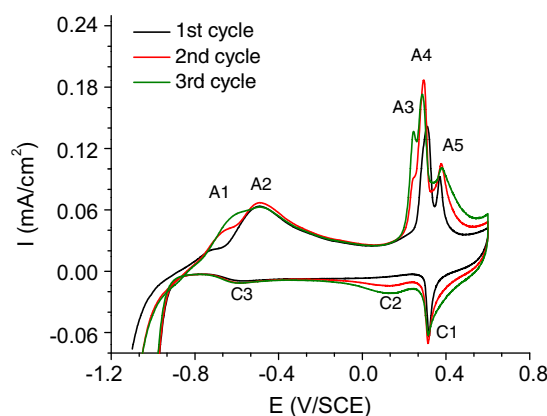
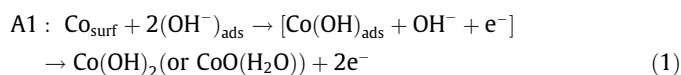
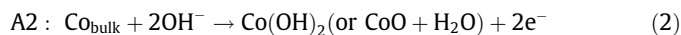


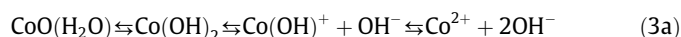
Fig. 4. Cyclic voltammograms obtained on Co. The CVs were recorded at a scan rate of 5 mV s^{-1} .



Peak A2 appears at potentials higher than the E_{eq} and it is assigned to the process:



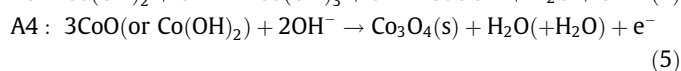
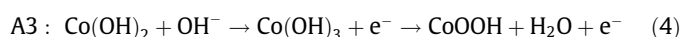
The Co^{II} species at, or very near, the metal surface will be hydrated. The hydrated Co^{II} is in acid–base equilibrium with hydroxides:



The hydrated species can dissolve from the metal/oxide interface where they can diffuse into the aqueous phase or precipitate (and/or condense) back onto the metal to form a solid $\text{CoO}/\text{Co}(\text{OH})_2$ film. Once a solid phase film is formed, reaction (2) may continue by the injection of Co^{II} into the oxide phase at the metal/oxide interface. This is balanced by injection of OH^- (or O^{2-}) into the oxide phase at the oxide/water interface.

Peak A2 is located at a higher potential because there is a slight barrier to overcome to oxidize the Co atoms in the bulk metal. This barrier is independent of the oxide surface state and we observe that the magnitude of peak A2 is independent of the number of CVs that have been performed on a sample. On the other hand, the magnitude of peak A1 increases with scan-cycle number. This behavior can be attributed to a process associated with Co at the metal surface where the reactive surface area and number of reactive sites are modified by the potential history of a metal.

The growth of the Co^{II} oxide/hydroxide layer passivates the surface and the current decreases. At potentials above $0.1 V_{\text{SCE}}$, where the oxidation of Co^{II} to either Co_3O_4 or CoOOH is thermodynamically allowed (Fig. 3), the current increases again. The anodic formation of CoOOH should be kinetically more favored than formation of Co_3O_4 since it requires less structural rearrangement of the oxide; it only requires dehydration following the oxidation of $\text{Co}^{\text{II}}\text{--Co}^{\text{III}}$ in the hydroxide form. Thus, peak A3 (Fig. 4) is assigned to the oxidation of hydrated $\text{Co}(\text{OH})_2$ to CoOOH at or near the oxide/water interface (reaction (4)). Peak A4, located at a slightly higher voltage is attributed to the conversion of $\text{CoO}/\text{Co}(\text{OH})_2$ in the bulk solid phase to a mixed $\text{Co}^{\text{II/III}}$ oxide (Co_3O_4) (reaction (5)):

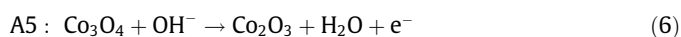


Peak A3 is barely visible on the first CV scan and increases in intensity with scan-cycle number. The height of peak A3 is initially low because reaction (4) will be limited to conversion of a hydrated surface layer. The surface coverage and/or thickness of this layer increases with scan cycle as reaction (1) becomes more important.

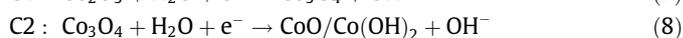
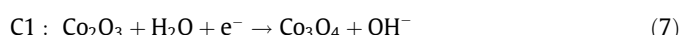
Alternative assignments of peaks A3 and A4 could be to the oxidation of two different solid phases of $\text{Co}(\text{OH})_2$ that are known to exist: $\alpha\text{-Co}(\text{OH})_2$, which consists of four ordered $\text{Co}(\text{OH})_2$ layers followed by one less-ordered $\text{Co}(\text{OH})_2$ layer, and $\beta\text{-Co}(\text{OH})_2$, which has an ordered CdI_2 structure in which the anions form a cubic close-packed structure while the cations occupy all of the octahedral interstices [16]. Feitknecht observed that $\alpha\text{-Co}(\text{OH})_2$ was susceptible to oxidation to CoOOH and that this oxidation occurred topochemically without the formation of a new phase and a requirement for a nucleation phenomena [17]. Foelske and Strehblow [16] later suggested that intercalated water may be responsible for the $\sim 3.4 \text{ \AA}$ larger c -axis in the $\alpha\text{-Co}(\text{OH})_2$ crystal lattice than in the $\beta\text{-Co}(\text{OH})_2$ crystal lattice. We do not believe that oxidation of two different $\text{Co}(\text{OH})_2$ phases is important in our system. The

oxidation of $\alpha\text{-Co}(\text{OH})_2$ to CoOOH should be fast since it only requires that a proton leave the intercalated water layer, and this is consistent with the presence of reaction (4). The presence of Co_3O_4 in the oxide layer grown at potentials $>0.1 V_{\text{SCE}}$ was determined by XPS (see below) and this confirms that reaction (5) is also occurring.

At a higher potential ($0.4 V_{\text{SCE}}$) an additional peak, A5, is observed. The height of this peak behaves similarly to peak A4 as a function of scan-cycle number, but peak A5 broadened with increased cycling and its corresponding reduction peak, C1, showed near reversible behavior. Peak A5 is assigned to the conversion of the $\text{Co}^{\text{II/III}}$ oxide (Co_3O_4) to a Co^{III} oxide (Co_2O_3):



The reduction peaks C1 and C2 are assigned to reactions (7) and (8), respectively:



The near reversibility of peaks A5 and C1 suggests that kinetically facile oxidation and reduction of Co^{II} and Co^{III} is occurring in the oxide lattice. Crystalline Co_3O_4 has a normal spinel structure with Co^{III} occupying the octahedral sites and Co^{II} the tetrahedral sites [8]. Although the structure of the meta-stable Co_2O_3 is less well established, anodic oxidation in a spinel oxide is known to occur easily [22] due to its spacious lattice structure; Co_3O_4 is a p-type semiconductor with a small band gap in the range of 1.4–1.8 eV [8]. Similar reversible oxidation/reduction behavior has been observed for the conversion between Fe_3O_4 and $\gamma\text{-Fe}_2\text{O}_3$, both of which share a spinel structure (inverse spinel for magnetite) [22]. The broadening of peaks A5 and C1 with increasing scan-cycle number can be attributed to an increase in the reactive surface sites as the cycling increases.

Peak C3 was observed only when the upper scan limit of a CV was higher than $0.1 V_{\text{SCE}}$ and, hence, the assignment of this peak to the reduction of Co^{II} species is ruled out. Rather, this peak is assigned to the reduction of CoOOH to $\text{Co}(\text{OH})_2$:



This assignment is consistent with the study by Behl et al. [9] which showed that the oxidation of $\text{Co}(\text{OH})_2$ to CoOOH occurs readily, but the reduction of CoOOH to $\text{Co}(\text{OH})_2$ is very slow.

In summary, the CV results show three potential regions of anodic oxidation of Co at pH 10.6:

Region I ($E < -0.7 V_{\text{SCE}}$): This region lies below the equilibrium potential for the Co to $\text{CoO}/\text{Co}(\text{OH})_2$ reaction and no bulk Co oxidation is observed (or expected) in this region.

Region II ($-0.7 V_{\text{SCE}} < E < 0.1 V_{\text{SCE}}$): Oxidation of Co in the bulk metal phase is limited to the formation of $\text{CoO}/\text{Co}(\text{OH})_2$.

Region III ($E > 0.1 V_{\text{SCE}}$): Oxidation of Co to Co^{II} oxide/hydroxide continues but the Co^{II} formed is also further oxidized to less soluble $\text{Co}^{\text{II/III}}$ and/or Co^{III} oxides/hydroxides.

The division of the oxidation processes into three potential regions is in good agreement with previous studies on Co in a mildly basic solution (pH range of 9.3–12) [6,10,11]. Those studies also concluded that two types of passive layers are formed in alkaline solutions; a layer formed at low potentials that consists of CoO and a layer formed at high potentials that consists of CoOOH and Co_3O_4 on top of an inner layer of CoO [6,10].

The corrosion potential of Co without ionizing radiation present is measured at $-0.7V_{\text{SCE}}$ to $-0.6V_{\text{SCE}}$ (Fig. 2), a value at or slightly higher than the transition potential between regions I and II (i.e., the equilibrium potential for the Co to $\text{CoO}/\text{Co}(\text{OH})_2$ reaction). In contrast, E_{CORR} with 5.5 kGy h^{-1} ionizing radiation present ($0.08 V_{\text{SCE}}$, Fig. 2) is at the transition between regions II and III.

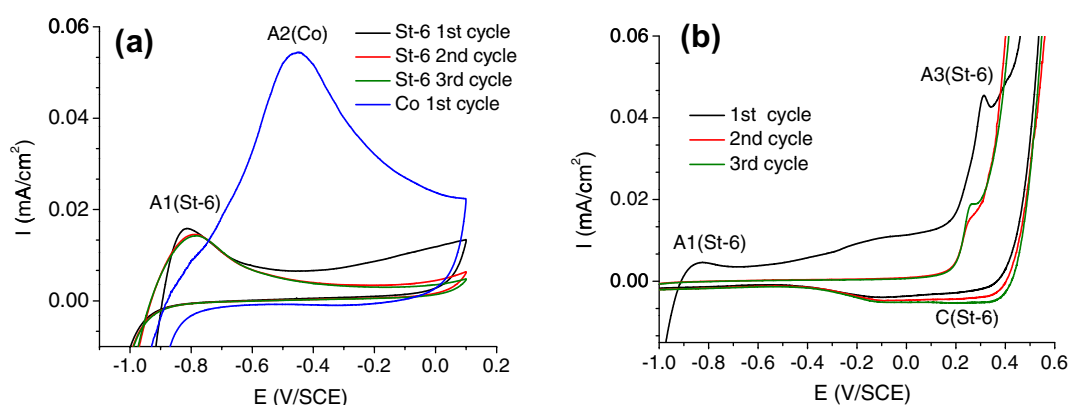
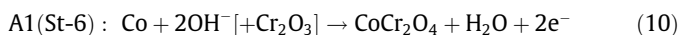


Fig. 5. Cyclic voltammograms recorded on Stellite-6 for two potential scan ranges from. (a) $-1.1 V_{SCE}$ to $0.1 V_{SCE}$, and (b) $-1.1 V_{SCE}$ to $0.6 V_{SCE}$. The first cycle of a CV recorded on Co is also shown in (a) for comparison.

3.2.1.2. Stellite-6. Cyclic voltammograms recorded on Stellite-6 are shown in Fig. 5; two different scan ranges were used, $-1.1 V_{SCE}$ to $0.1 V_{SCE}$ and $-1.1 V_{SCE}$ to $0.6 V_{SCE}$. Also shown in Fig. 5a is the first cycle of a CV performed on Co for comparison. The first anodic peak (labeled A1(St-6) for Stellite-6) in Fig. 5a appears at a much lower potential than the first peak seen on Co (A2(Co)). At this potential, Co oxidation to Co^{II} oxide/hydroxide is not thermodynamically allowed potentials. However, the equilibrium potentials for the oxidation of Cr to Cr^{III} ($CrOOH$ and Cr_2O_3) lie below $-1.4 V_{SCE}$. The Stellite-6 surface is initially covered by a thin, air-formed Cr^{III} oxide and this oxide is not completely removed during the electrode cathodic treatment before the first CV. Peak A1(St-6) can therefore be attributed to the oxidative injection of Co^{II} into the chromium oxide layer, leading to conversion of that layer to cobalt chromite, $CoCr_2O_4$. This is followed by formation of a Co^{II} oxide/hydroxide outer layer at higher potentials:



Chromium oxide, Cr_2O_3 , being a p-type semi-conductor with a large band gap of 3.4 eV [23], is ionically insulating at low potentials and, therefore, its presence should significantly impede the further oxidation of an underlying metal. However, the air-formed chromium oxide is likely defective, and the Co^{II} ion is thermodynamically stable in a chromite at potentials above $-1.1 V_{SCE}$ (Fig. 3). When the Cr^{III} oxide layer is saturated with Co^{II} and a potential greater than $-0.7 V_{SCE}$ is applied, additional Co^{II} can migrate through the oxide layer to the chromite/water interface where it can be hydrated and subsequently condense to grow an outer layer of $CoO/Co(OH)_2$ or diffuse into the aqueous phase. Consequently, we see the presence of both $CoCr_2O_4$ and $CoO/Co(OH)_2$ in an oxide potentiostatically grown at $-0.7 V_{SCE}$ (see XPS results below).

The presence of a $CoCr_2O_4$ layer adds a barrier to cation migration that is not present in pure Co and this explains why the electrochemical reactivity of the Stellite-6 surface is much lower than that of the Co surface (lower anodic current densities) at potentials $>-0.6 V_{SCE}$ (see further discussion below).

With an upper scan limit of $0.1 V_{SCE}$, the onset of peak A1(St-6) appears at a lower potential in the first cycle than in subsequent cycles (Fig. 5a). Stable Cr_2O_3 has a corundum crystal structure while stable $CoCr_2O_4$ has a spinel structure [24]. Injection of Co into the Cr_2O_3 oxide lattice requires energy sufficient to induce the required changes to the oxide lattice structure. When the upper limit of the potential scan is increased to $0.6 V_{SCE}$, the anodic current density seen near $-0.7 V_{SCE}$ is much reduced in the second and higher number of CV cycles compared to that of the first cycle (Fig 5b). This is because of changes to the chromium oxide that occur at

higher potentials. At potentials $>0.3 V_{SCE}$, Cr^{III} can oxidize to Cr^{VI} which can readily dissolve in water. This dissolution removes the chromite layer. A more coherent and compact Cr_2O_3 oxide layer than the initial defective layer forms after the first CV cycle and this more insulating layer inhibits Co^{II} migration. Consequently, the Stellite-6 CVs cycles over the potential range -1.1 to $0.6 V_{SCE}$ are very different for cycle 1 and subsequent CV cycles, and the latter do not show any further anodic current at low potentials.

The CV of Stellite-6 in Fig. 5b shows that the anodic current increases again at potentials above $-0.6 V_{SCE}$ (first cycle) and above $0.2 V_{SCE}$ for subsequent cycles. In the potential range $-0.6 V_{SCE}$ to $0.1 V_{SCE}$, the growth of the outer $CoO/Co(OH)_2$ layer continues. The anodic current in this region increases nearly linearly with potential during the scan and this is attributed to a linear growth in the thickness of the outer $CoO/Co(OH)_2$ layer. The impact of the increasing potential is balanced by a commensurate increase in the ohmic resistance of the oxide layer as it thickens. As the potential is scanned above $-0.2 V_{SCE}$, the current stays nearly constant with potential and this behavior is attributed to control of the reaction rate by diffusion of OH^- to the surface. No anodic current is seen in this potential region for scan cycles greater than 1 because of the presence of the insulating Cr_2O_3 oxide layer.

Since electrode potentials in the range 0.1 and $0.3 V_{SCE}$ are not high enough to support anodic dissolution of chromium (by oxidizing insoluble Cr^{III} to soluble Cr^{VI}) [25], the anodic current in this potential range is due to the oxidation of cobalt species, see reactions (4), (5) and (6). The rates of these reactions are much slower on Stellite-6 than on Co due to the presence of the cobalt chromite inner layer.

At potentials above $0.3 V_{SCE}$, where Cr^{III} can be easily oxidized to highly soluble Cr^{VI} oxides, the anodic current increases rapidly with potential. In this high potential region, the oxidative dissolution of chromium dominates the anodic current behavior. On the return CV sweep, the reduction current begins to flow almost immediately and is distributed over a very wide potential range, down to about $-0.3 V_{SCE}$ (peak C(St-6)). The broad cathodic feature, labeled C(St-6) in Fig. 5b, probably comprises the processes included in both peaks C1 and C2 on Co (Fig. 4), but the separation into two peaks is lost, perhaps due to the influence of chromium oxides on the film conversion kinetics [13] and also the reduction of any Cr^{VI} species that were still retained with the film at the of anodic CV sweep.

In summary, the CV results for Stellite-6 show that oxidation behavior can be divided into four potential regions at pH 10.6. These regions are almost identical to the regions identified for Co oxidation (with the differences in the transition between Region I

and Region II matching the differences in the values of E_{CORR} for the metals. Stellite-6 has an extra region at high potentials to account for Cr oxidation.

Region I ($E < -0.6 V_{\text{SCE}}$): In this region the oxidation of Co to Co^{II} converts the pre-existing chromium oxide layer to cobalt chromite.

Region II ($-0.6 V_{\text{SCE}} < E < 0.1 V_{\text{SCE}}$): The oxidation of Co to Co^{II} continues. When the chromite layer becomes saturated with Co^{II} , $\text{CoO}/\text{Co}(\text{OH})_2$ is formed at the oxide/water interface. The rate of anodic oxidation in this region is much lower on Stellite-6 than on Co.

Region III ($0.1 V_{\text{SCE}} < E < 0.3 V_{\text{SCE}}$): In this region Co^{II} oxide/hydroxide is continuously formed and it is also further oxidized to less soluble $\text{Co}^{\text{III/IV}}$ and/or Co^{III} oxides/hydroxides.

Region IV ($E > 0.3 V_{\text{SCE}}$): The oxidative dissolution of chromium becomes the dominant anodic process.

Like the cobalt system, E_{CORR} of Stellite-6 without ionizing radiation present is about $-0.47 V_{\text{SCE}}$, a value slightly higher than the transition between regions I and II, whereas with ionizing radiation present E_{CORR} is about $0.12 V_{\text{SCE}}$, a value at the transition potential between regions II and III.

3.3. Oxide formation and conversion under potentiostatic conditions

3.3.1. Experimental results and data analyses

Oxide formation was studied under potentiostatic conditions at three potentials, -0.7 , -0.2 and $0.2 V_{\text{SCE}}$ for both Co and Stellite-6. These potentials were chosen based on the electrochemical reactivity seen in CV scans. Additional potentiostatic experiments were carried out on Stellite-6 at a number of applied potentials in the range from $0.1 V_{\text{SCE}}$ to $0.4 V_{\text{SCE}}$. In the potentiostatic experiments, a desired potential, E_{APP} , was applied immediately after cathodically stripping the electrode at $-1.1 V_{\text{SCE}}$ for 5 min. The current was monitored as a function of time (typically up to 2 d) to obtain kinetic information on anodic oxidation processes occurring on the Co and Stellite-6 surfaces. Electrochemical impedance spectra (EIS) were recorded periodically during a potentiostatic test to characterize the oxide films that were formed. Upon the conclusion of each experiment, the electrode was removed from the electrochemical cell and the surface was characterized using XPS. The XPS analysis provides information on the state of the metal surface after extended oxidation and the current vs. time plots and EIS spectra provide information on the film growth kinetics. The EIS spectra were modeled using electric equivalent circuits to derive the resistance and capacitance of the electrochemical systems. The XPS spectra were deconvoluted using standard reference spectra to determine the chemical composition and oxidation states of the metal atoms in the oxide layers.

The results of EIS measurements and analyses are discussed first because this aids in discussion of the other results. Representative EIS spectra, recorded on Stellite-6 during polarization at $0.2 V_{\text{SCE}}$, are shown in a Bode plot in Fig. 6a. The EIS spectra obtained during potentiostatic polarization at $-0.2 V_{\text{SCE}}$ and $0.2 V_{\text{SCE}}$ were analyzed using a modified Randles electric equivalent circuit model to extract the capacitive and resistive characteristics of the films formed on the surfaces. An electric equivalent circuit analysis of the EIS obtained at $-0.7 V_{\text{SCE}}$ was not performed due to the large water reduction currents observed for both Co and Stellite-6 surfaces at this potentials.

In our work, the Co and Stellite-6 surfaces contain several oxide phases that are not distinct and, hence, their individual RC components are not easily separated. Thus, a simple Randles-type circuit consisting of one RC (resistor–capacitor) component in series with the resistance of the solution, R_s , was used to model the oxide layer as a whole. A constant phase element (CPE) was used in place of the capacitor for the EIS analysis. A more complex equivalent circuit model could be used but, since there is no unique solution to a least squares fit to our EIS data, this was not done. The Randles-type circuit provides a good fit to our EIS data, as shown in Fig. 6b. The CPE accounts for non-idealities (i.e., frequency dispersion) in the capacitive response of the system. The exponent of the CPE, α , derived from fitting this circuit model to the data, was in the range of 0.8–0.85, indicating that the electrode possessed a very capacitor-like interface (a value of 1 applies to a pure capacitor). The CPE parameters were converted to capacitance values using the method of Brug et al. [26]. The resistance and capacitance values obtained from fitting the EIS data are shown in Fig. 7. Although the polarization (or system) resistance, R_p , is theoretically composed of a film resistance, R_{film} , and an interfacial charge transfer resistance, R_{ct} , in series with one another, the equivalent circuit analysis of the EIS data could not resolve the contributions of R_{film} and R_{ct} or those of different oxide films, so the additive polarization resistance R_p is plotted in Fig. 7.

X-ray photoelectron spectroscopy (XPS) was used to characterize the chemical states of Co and Cr in the oxide films. Both low resolution (or survey) spectra and high resolution spectra in the Co 2p, Cr 2p, and O 1s regions were used. The ratio of Co to Cr in the Stellite-6 films was obtained from the relative areas of the Co 2p peak at 780 eV and the Cr 2p peak at 574 eV in the survey spectra. To determine the oxidation state(s) of Co atoms in a film, the high resolution spectra of the Co 2p band were deconvoluted using reference spectra for single-phase Co^0 , $\text{Co}(\text{OH})_2$, CoO , Co_3O_4 , CoOOH , and CoCr_2O_4 (with binding energies of 778.1, 780.4, 780.0, 779.6, 780.1 and 778.8 eV, respectively) [17]. A representa-

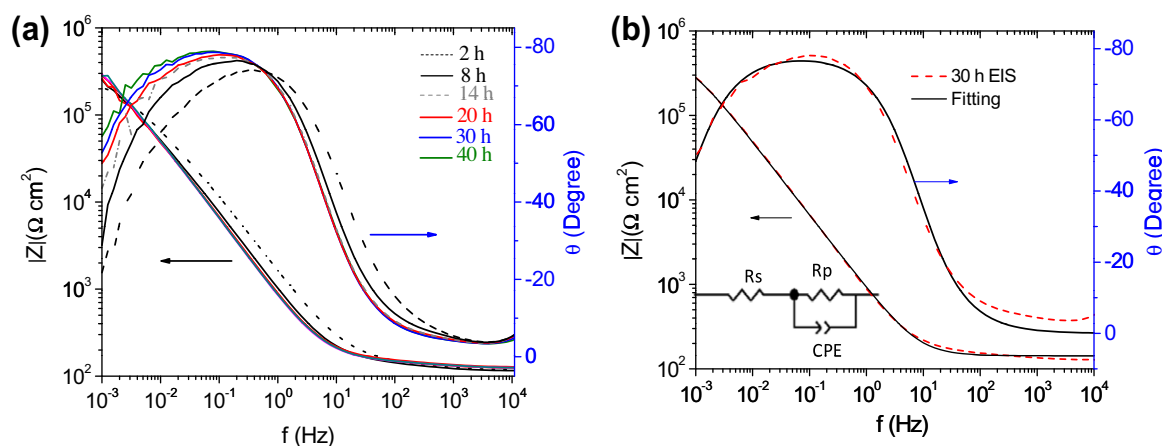


Fig. 6. Electrochemical impedance spectra recorded at various times during film growth at $0.2 V_{\text{SCE}}$ on Stellite-6. (a) Bode plots of the impedance magnitude and phase angle and (b) One example of a model fit to an observed spectrum. The equivalent circuit used for the EIS analysis is shown inset.

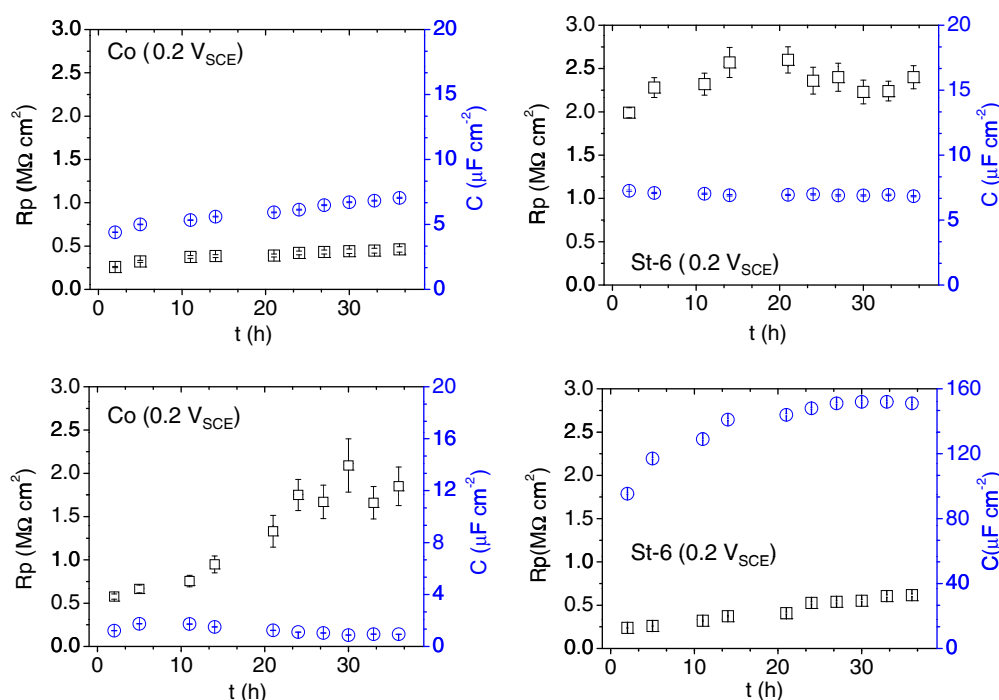


Fig. 7. Polarization resistance (■) and capacitance (○) as a function of time during potentiostatic film growth at $-0.2 V_{SCE}$ (upper figures) and $0.2 V_{SCE}$ (lower figures) on Co and Stellite-6. The resistance and capacitance values were obtained from fits to EIS spectra using the equivalent circuit model shown in the inset of (b). The error bars include only the model-fitting errors which in most cases are smaller than the sizes of the symbols representing the data.

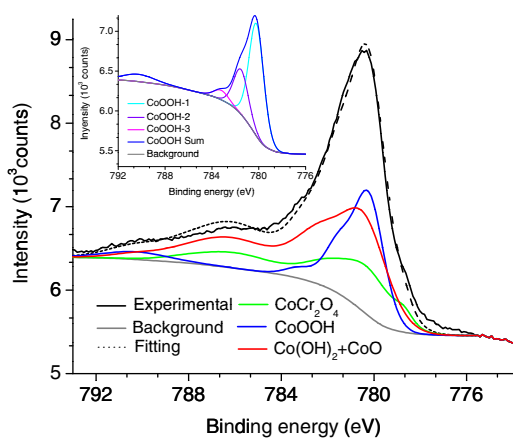


Fig. 8. High resolution XPS spectrum of the Co 2p band (and its deconvoluted components) for a film grown at $0.15 V_{SCE}$ on Stellite-6. The inset shows the CoOOH spectrum consisting of multiple peaks.

tive high resolution spectrum of the Co 2p band and its deconvolution into oxide contributors is shown in Fig. 8 for a film grown at $0.15 V_{SCE}$ on Stellite-6. Some of the reference spectra contain multiple peaks, for example, the CoOOH spectrum is composed of multiple peaks as shown in the inset of Fig. 8. For Cr speciation, high resolution spectra of the Cr 2p (~ 575 eV) region were deconvoluted using reference spectra for single-phase Cr^0 , Cr_2O_3 , $CoCr_2O_4$, and $Cr(OH)_3$ (binding energies of 574.2, 575.7, 575.2 and 577.3 eV, respectively) [17,27]. The deconvolution of an XPS band using multiple-peak reference spectra with a Shirley-type background subtracted has previously been successfully applied to cobalt oxide samples by Biesinger et al. [17,27]. A weighted-composite peak was constructed and compared with the observed peak, see Fig. 8. Commercial software (CASAXPS®) was used for

the fitting analysis. The weighting factors accounts for the relative concentration of each particular species in an oxide film.

The results of the XPS fitting analysis for films grown on pure Co and Stellite-6 are summarized in Figs. 9 and 10, respectively. Note that in Fig. 9a only the fractions of Co metal and Co_3O_4 in the Co 2p peak are shown. The dominant contributor at all potentials (balance $Co(OH)_2$) is not shown in order to present the contributions of the two minor components of the Co oxide film more clearly.

3.3.2. High-purity Co

3.3.2.1. Film growth at $-0.7 V_{SCE}$. The time dependent behavior of current as a function of time at constant potential is shown in the $\log |i|$ versus $\log t$ plots in Fig. 11a. During potentiostatic polarization at $-0.7 V_{SCE}$, the current initially decreases linearly with time (i.e., the slope of the $\log |i|$ vs. $\log t$ plot is -1) but switches in sign from anodic to cathodic at ~ 100 s (Fig. 11a). The linear decrease in the anodic current within 100 s indicates that the nature of the oxide formed on Co does not change during this time. This is consistent with growth of a Co^{II} oxide/hydroxide layer at a constant rate at this potential (reaction 1). The solubility of $Co(OH)_2$ is at its minimum at pH 11 (~ 1 M) [11,15] and a uniform solid phase of Co^{II} oxide/hydroxide quickly covers the surface. The current density decreases steadily as the oxide thickens.

At ~ 100 s the current becomes cathodic and its magnitude quickly reaches a steady-state value (constant for the rest of the potentiostatic experiment). Cobalt oxide/hydroxide is known to be electronically conducting [12]. Although it is a p-type semiconductor it has a small band gap of 2.4 eV and a photocurrent can be easily generated by room fluorescent lighting (the experiments were not conducted in the dark). The negative current is attributed to reduction of aqueous species on this electronically conducting surface, possibly driven a photo-process. This process is hidden at first by the overriding anodic reaction and only becomes observable when the anodic reaction rate decreases sufficiently. We did not fully investigate the contribution of a photocurrent fully, but

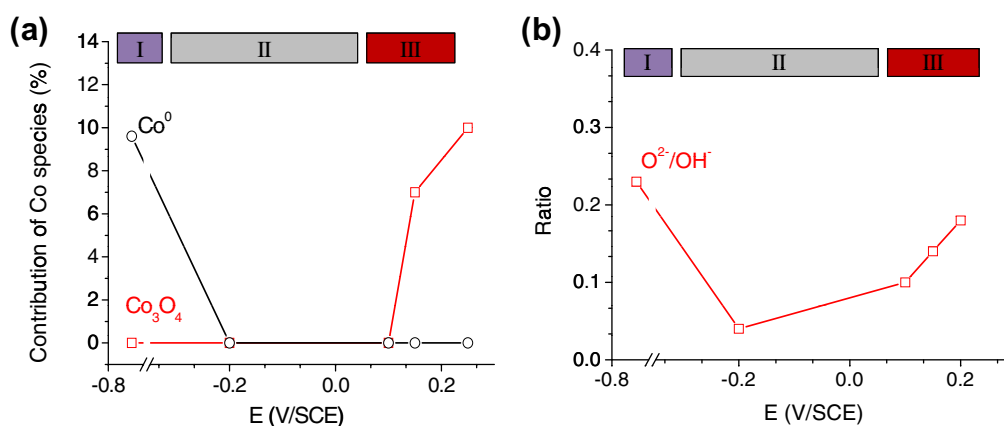


Fig. 9. Speciation on the surface of Co as a function of applied potential determined by the XPS analysis: (a) Co oxides and (b) $\text{O}^{2-}/\text{OH}^-$.

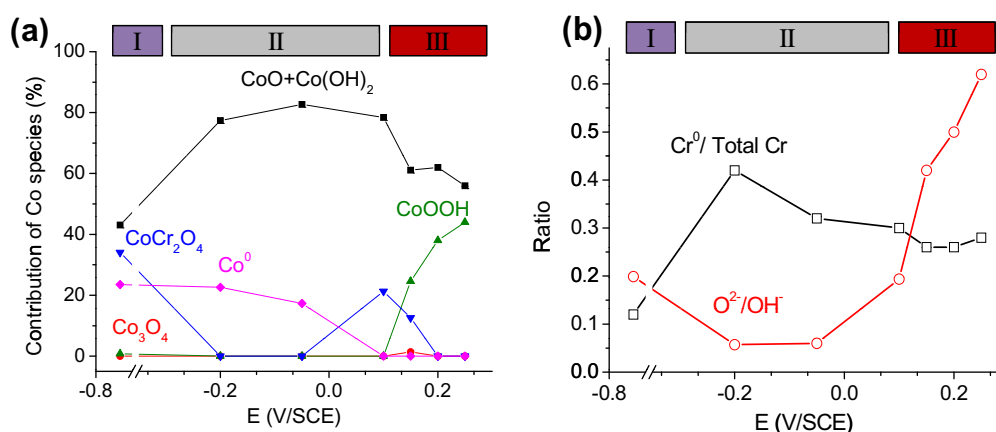


Fig. 10. Speciation on the surface of Stellite-6 as a function of applied potential determined by the XPS analysis: (a) Co oxides, and (b) ratios of metallic Cr/total Cr, and $\text{O}^{2-}/\text{OH}^-$.

limited tests in a darkened laboratory showed a reduction in the cathodic current level.

The XPS analysis of the film formed at $-0.7 \text{ V}_{\text{SCE}}$ (Fig. 9a) shows a substantial contribution of a metal atom component (Co^0) to the Co 2p peak ($\sim 10\%$). This component comes from the bulk metal that underlies the surface oxide and indicates that the oxide film is less than 10 nm thick (the depth analysis range of the XPS instrument). The remaining contribution to the Co 2p band is from $\text{CoO}/\text{Co}(\text{OH})_2$. Analysis of the high resolution O 1s peak shows a high contribution from OH^- (Fig. 9b) indicating that Co^{II} is present mostly in the hydroxide form ($\text{Co}(\text{OH})_2$).

3.3.2.2. Film growth at $-0.2 \text{ V}_{\text{SCE}}$. During potentiostatic polarization at $-0.2 \text{ V}_{\text{SCE}}$, the current is initially high at $\sim 3 \text{ mA cm}^{-2}$ and remains nearly constant for a short duration (Fig. 11a). The current then drops abruptly and subsequently decreases linearly with time from this new, lower current level to reach a very low value of 60 nA cm^{-2} after $\sim 10^5 \text{ s}$ ($\sim 1 \text{ d}$). At this potential the rate of Co to Co^{II} oxidation at the metal/water interface is initially very high due to large overpotential. The high short-term current can be attributed to the fact that the oxidation of Co to Co^{II} is limited not by the rate of interfacial charge transfer but by the diffusion of charged species (metal cations and aqueous ions, H^+ and OH^-) through the Helmholtz or double layer (or the interfacial region). The rate of movement of charged species through the double layer depends on the electric field potential gradient across the layer. Injection of a large amount of Co^{II} can result in a significant iR drop

across into the interfacial region and can slow down the diffusion of the charged species [28].

When the concentration of Co^{II} species in the interfacial region reaches its solubility limit, the Co^{II} species precipitate and condense into a solid phase oxide/hydroxide. With this solid film present the oxidation rate is limited by the rates of interfacial charge transfer and/or ion transport through the oxide. Thus, the rapid formation of a uniform layer of Co^{II} oxide/hydroxide causes a sudden drop in the current.

Once a uniform coherent oxide layer is formed, the anodic oxidation rate of Co to Co^{II} is determined by the rate of interfacial charge transfer at the metal/oxide and oxide/water interfaces and the rate of Co ion migration through the oxide layer. The Co^{II} produced can either be incorporated into the growing the oxide layer or be transported to the oxide/water interface where it can be hydrated and dissolve into the aqueous phase. The linear decrease in the anodic current with time suggests the current is mainly due to oxide growth and that the dissolution current is small. As the oxide layer thickens anodic oxidation slows and the anodic oxidation rate approaches the rate of dissolution of the Co cation from the oxide surface. The system eventually reaches a steady-state balance between the rates of Co oxidation and Co dissolution and the oxide layer no longer grows. As expected, at long times the anodic current is higher for the higher applied potential.

The current on an electrode during the linear decrease period was about an order of magnitude higher during polarization at $-0.2 \text{ V}_{\text{SCE}}$ than that seen at $-0.7 \text{ V}_{\text{SCE}}$ (Fig. 11a). This higher current

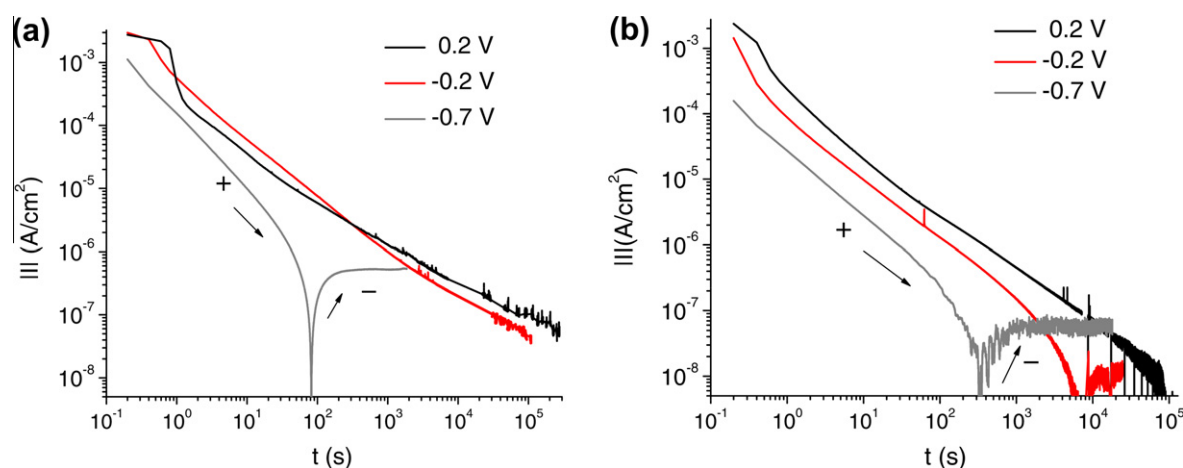


Fig. 11. Current as a function of time observed during potentiostatic film growth at -0.7 , -0.2 , and 0.2 V_{SCE} , on (a) Co, and (b) Stellite-6. The + and – signs indicate anodic and cathodic currents, respectively.

can support the growth of a thicker film. This is consistent with the XPS results (Fig. 9a) which show the presence of a thicker Co^{II} oxide/hydroxide layer on an electrode treated at -0.2 V_{SCE} compared to the layer on an electrode treated at -0.7 V_{SCE} .

The equivalent electric circuit analysis of the EIS taken at -0.2 V_{SCE} (Fig. 7) yielded a polarization resistance value that is relatively low (initially ~ 0.2 $M\Omega\text{ cm}^2$ and increasing to a steady-state value of ~ 0.5 $M\Omega\text{ cm}^2$ after 2 h). The increase in R_p is accompanied by decrease in the system capacitance from ~ 4 $F\text{ cm}^{-2}$ to ~ 7 $F\text{ cm}^{-2}$. The increase in resistance can be caused by either a thickening of an oxide film or the conversion of an existing film to a more insulating oxide. The increase in capacitance can be caused by either a decrease in film thickness, an increase in electrode surface area, or an increase in the dielectric constant of the oxide film. The XPS results (Fig. 9a) shows that only $CoO/Co(OH)_2$ is present (within the analysis depth of 10 nm). The increase in resistance is attributed to the thickening of this oxide and the increase in capacitance is attributed to an increase in the active electrode surface area as the oxide grows. An SEM image of the surface (not presented) shows the presence of a filiform layer. This physical structure has an active surface area that is much larger than the geometric area of the electrode coupon. Growth of this type of structure is consistent with an increase in the active surface area of a $CoO/Co(OH)_2$ oxide layer.

3.3.2.3. Film growth at 0.2 V_{SCE} . The current observed during polarization at 0.2 V_{SCE} shows similar behavior to the current observed at -0.2 V_{SCE} (Fig. 11a). The initial current is the same, but the duration of near constant current lasts longer at 0.2 V_{SCE} . This short-term behavior is attributed to the same phenomena discussed above for the polarization at -0.2 V_{SCE} . The current remains longer at a higher potential because the diffusion of charged species through the double layer will be prolonged by the higher potential gradient in the interfacial region. The larger current drop at 0.2 V_{SCE} than at -0.2 V_{SCE} is attributed to the formation of a thicker oxide at this potential as more Co^{II} species accumulate in the oxide layer over the longer cation diffusion length.

Following a sudden initial current drop, the current decreases linearly. Again, this is consistent with the growth of a thicker oxide layer. However, the current at 0.2 V_{SCE} actually drops below the current seen at -0.2 V_{SCE} for some time, but then the situation reverses after ~ 500 s. The XPS results (Fig. 9) show that the oxide layer formed at 0.2 V_{SCE} the film consists of both Co^{II} oxide/hydroxide and Co_3O_4 while the film formed at -0.2 V_{SCE} consists of only $CoO/Co(OH)_2$. We attribute the lower current at 0.2 V_{SCE} at

intermediate times to the early growth of a thicker oxide film. At longer times the current at 0.2 V_{SCE} becomes greater than that at -0.2 V_{SCE} as the oxidation of Co^{II} to Co_3O_4/Co_2O_3 contributes more to the total current. The Co 2p band in the XPS spectra were successfully deconvoluted without any contribution from Co_2O_3 . The reference spectrum of this oxide was not available and, hence, it was not included in the XPS deconvolution. The oxidation of Co_3O_4 to Co_2O_3 is kinetically facile at potentials above the equilibrium potential for the redox pair (0.23 V_{SCE} , shown in Fig. 3). However, since Co_2O_3 is both insulating and insoluble, it will form a very thin outer layer on the oxide surface. It is unsurprising that its omission in the Co 2p band deconvolution was not a problem.

At 0.2 V_{SCE} , the polarization resistance is initially low (~ 0.5 $M\Omega\text{ cm}^2$) at 2 h, but it increases steadily with time, reaching a value of ~ 2 $M\Omega\text{ cm}^2$ after 30 h (Fig. 7). The rate of increase is slow in the first 10 h while the dominant anodic process is conversion of $CoO/Co(OH)_2$ to Co_3O_4 . However, at longer times the resistance increases more rapidly due to the conversion of the Co_3O_4 to more insulating and less soluble Co_2O_3 . At the same time, the capacitance shows only slight decreases.

3.3.3. Stellite-6

3.3.3.1. Film growth at -0.7 V_{SCE} . At -0.7 V_{SCE} , the current behavior observed on Stellite-6 is very similar to that on Co (Fig. 11b); the current decreases nearly linearly with time and it switches from anodic to cathodic at ~ 300 s. The current during potentiostatic polarization on Stellite-6 is, however, about an order of magnitude lower than the current seen on Co under the same conditions. This is opposite to the current behavior observed during a CV scan; the current at -0.7 V_{SCE} is higher on Stellite-6 than on Co. The current observed at this potential during the CV scan corresponds to the oxidation of Co to Co^{II} to form cobalt chromite. During long-term polarization the conversion of the pre-existing thin layer of Cr^{III} oxide to $CoCr_2O_4$ is completed in a very short time and the current at longer times is due to anodic oxidation of Co to form a Co^{II} oxide/hydroxide layer. The current due to the latter anodic process is lower on Stellite-6 than on Co during at long times because of the presence of a passive inner layer of chromite on Stellite-6. Water reduction also occurs on Stellite-6 but the reduction current is lower than on Co because of the presence of the passivating chromite layer. Also less photocurrent is expected for Stellite-6. Cobalt chromite is also a p-type semiconductor but it has a higher a band gap (3.4 eV) [24] than the band gap of $Co(OH)_2$ (2.4 eV).

The XPS analysis results for the Stellite-6 at -0.7 V_{SCE} (Fig. 10) show that Co^{II} is present mainly as cobalt chromite ($CoCr_2O_4$)

and to a smaller extent as Co^{II} oxide/hydroxide. The presence of Co^0 in the high resolution Co 2p band indicates that the film formed at $-0.7 V_{\text{SCE}}$ is very thin ($<10 \text{ nm}$).

3.3.3.2. Film growth at $-0.2 V_{\text{SCE}}$. The current at $-0.2 V_{\text{SCE}}$ shows a linear decrease with time (Fig. 11b). It reaches a very small value before the net current ($\sim 10^{-8} \text{ A cm}^{-2}$) becomes cathodic after $\sim 2 \text{ h}$. Since this cathodic current is very low, it could be generated by several contributing processes, all of which are slow. Potential contributors include water reduction and reduction of trace dissolved oxygen in the alloy, possibly assisted by photo-induced reactions. The oxidative conversion of the pre-existing chromium oxide layer to a cobalt chromite layer occurs early and the linear behavior of the current vs. time is attributed to steady growth of CoO/Co(OH)_2 . The current at $-0.2 V_{\text{SCE}}$ is about an order of magnitude higher than the current at $-0.7 V_{\text{SCE}}$ and this is consistent with the growth of a thicker outer layer of Co^{II} oxide/hydroxide at this potential.

The XPS analysis results (Fig. 10) are also consistent with a thicker growth of CoO/Co(OH)_2 on an inner chromite layer. The XPS Co 2p spectrum is dominated by the CoO/Co(OH)_2 contribution for the films grown at $-0.2 V_{\text{SCE}}$ (and $-0.1 V_{\text{SCE}}$ which is also in potential region II) and the chromite contribution is below the XPS detection level. However, the metal Co^0 peak still contributes to the Co 2p band, indicating that the oxide layer is still thinner than 9 nm at this potential.

The EIS analysis of the film growth at $-0.2 V_{\text{SCE}}$ (Fig. 7) shows that the polarization resistance is $2.0\text{--}2.5 \text{ M}\Omega \text{ cm}^2$ and relatively independent of time. This is consistent with the presence of a passive chromite layer on Stellite-6. The resistance is already high at the time of the first EIS measurement (2 h) due to the presence of the chromite layer. The resistance increases only slightly with time (from 2.0 to $2.5 \text{ M}\Omega \text{ cm}^2$) and the capacitance remains nearly constant at $\sim 6 \text{ F cm}^{-2}$, which attests to the steady-state nature of the outer Co^{II} oxide/hydroxide layer.

3.3.3.3. Film growth in potential range of $0.1\text{--}0.4 V_{\text{SCE}}$. Since the electrochemical reactivity of Stellite-6 is high at potentials $>0.1 V_{\text{SCE}}$ (Fig. 5b) and E_{CORR} increases to a value greater than $0.1 V_{\text{SCE}}$ when radiation is present (Fig. 2), the anodic oxidation and dissolution of Stellite-6 was explored at a number of potentials within potential regions III and IV. The potentiostatic polarization results are shown in Fig. 12. At all potentials $>0.1 V_{\text{SCE}}$ the current initially decreases nearly linearly with time. However, after times of about $10\text{--}100 \text{ s}$, the rate of current decrease slows and becomes nonlinear. The slowing of the current decrease occurs faster with higher applied

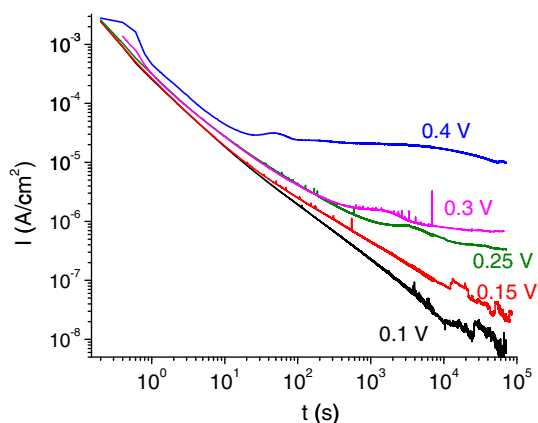


Fig. 12. Current as a function of time observed during potentiostatic film growth at $0.1, 0.15, 0.25, 0.3$ and $0.4 V_{\text{SCE}}$ on Stellite-6.

potentials. This change in behavior indicated the presence of more than one anodic process. Candidates include metal cation dissolution or further oxidation of an oxide that has already formed. At $0.4 V_{\text{SCE}}$, the current on Stellite-6 reaches a constant, value after only $\sim 10 \text{ s}$. The magnitude of this current ($30 \mu\text{A cm}^{-2}$) approaches a value expected for an aqueous diffusion-limited process at the electrode surface. At this potential, oxidation of insoluble Cr^{III} oxide to highly soluble Cr^{VI} oxide species is allowed and the high steady-state current at long times is attributed to this oxidation and chromium dissolution. This explanation is consistent with a potential dependent rate for chromium oxidation.

The presence of CoOOH in films grown at potentials $>0.1 V_{\text{SCE}}$ was found by the XPS (Fig. 10a). The fraction of CoOOH in the outer layer increases, while the fraction of CoO/Co(OH)_2 decreases, with an increase in the applied potential. The ratio of Co/Cr in the surface oxide also increases in this potential region, consistent with the loss of Cr from the oxide surface. No Co metal component of the Co 2p band was found showing that the oxides grown in this potential region are thicker than 10 nm despite the high rate of Cr dissolution.

Comparison of the XPS results for Co and Stellite-6 (Figs. 9a and 10a) shows that the Co^{III} species formed at potentials $>0.1 V_{\text{SCE}}$ on Stellite-6 is mainly CoOOH while it is mainly Co_3O_4 on Co. The presence of the chromite-like inner layer on Stellite-6 means that Co^{II} reaches the oxide/water interface at a slower rate and all of this Co^{II} can be subsequently oxidized to Co^{III} through the kinetically favored, formation of CoOOH . As discussed for reactions (5) and (6) in Section 3.2.1.1, the oxidation of Co(OH)_2 to CoOOH should be faster than the oxidation of Co(OH)_2 to Co_3O_4 .

At $0.2 V_{\text{SCE}}$, the polarization resistances the Stellite-6 films are lower and the capacitances are higher than the corresponding values derived for films grown at $-0.2 V_{\text{SCE}}$. At $0.2 V_{\text{SCE}}$, the Cr^{III} can begin to oxidize to Cr^{VI} , which is less protective, rendering the oxide film somewhat less protective, and decreasing its resistivity. The capacitance value ($\sim 150 \mu\text{F cm}^{-2}$) is independent of time and is an order of magnitude higher than that expected for a double-layer capacitance [13]. Since a potential of $0.2 V_{\text{SCE}}$ is high enough to drive cobalt oxidation and since the oxide layer on Stellite-6 at this potential has a mix of metal cation oxidation states, any change in the relative population of species in each oxidation state would change the net surface charge. For example, the oxidation of Co^{II} to Co^{III} can attract more OH^- to the oxide surface whereas the reduction of Co^{III} to Co^{II} repulses OH^- . This is equivalent to adsorbing and desorbing a high surface coverage of ions and leads to the storage of a large amount of charge in an extremely thin layer in the interfacial region. This is often referred to as pseudo-capacitance and is the probable explanation for the observed high capacitance value [14].

4. Conclusions

At pH 10.6 and room temperature, gamma-irradiation at a dose rate of 5.5 kGy h^{-1} increases the corrosion potential from $-0.7 V_{\text{SCE}}$ to $0.08 V_{\text{SCE}}$ on pure Co and from $-0.48 V_{\text{SCE}}$ to $0.12 V_{\text{SCE}}$ on Stellite-6. The corrosion behavior of Co and Stellite-6 can be divided into a number of potential regions and the presence of ionizing radiation shifts the corrosion potential from the transition between potential regions I and II to the transition between potential regions II and III for both metals. The transition from region I to II occurs near $-0.7 V_{\text{SCE}}$, the equilibrium potential for Co to CoO/Co(OH)_2 oxidation, while the transition from region II to III occurs at $\sim 0.1 V_{\text{SCE}}$, the equilibrium potential for CoO/Co(OH)_2 conversion to mixed $\text{Co}^{\text{II/III}}$ or Co^{III} oxides/hydroxides.

Due to the presence of a thin, defective Cr^{III} oxide layer on Stellite-6, the oxidation of Co to Co^{II} starts at a lower potential on Stellite-6 than on Co. The Co^{II} produced at potentials lower than

–0.7 V_{SCE} is incorporated into the Cr^{III} oxide layer on Stellite-6 and forms cobalt chromite (CoCr₂O₄). The chromite layer on Stellite-6 also suppresses the electrochemical reactivity of this alloy at higher potentials. The same cobalt oxidation reactions occur on Stellite-6 as on Co, but at much slower rates for a given potential. Gamma-irradiation increases the corrosion potential of both metals to a range where the rate of oxidation of Co to Co^{II} increases. This Co^{II} can further oxidize to form less soluble Co^{III} species. The competition of these two reactions (oxidation of Co to Co^{II} and oxidation of Co^{II} to Co^{III}) determines the net effect of gamma radiation on the rate of Co dissolution from Stellite-6. Solution pH and temperature have a strong influence on oxide solubilities. Additional work to investigate influence of these parameters on Stellite corrosion is currently underway.

Acknowledgments

This research was funded under the Natural Science and Engineering Council of Canada (NSERC) and Atomic Energy of Canada Limited (AECL) Industrial Research Chair Agreement. The electrochemical analysis equipment was purchased using a Grant from the Canada Foundation for Innovation. Surface Science Western is greatly acknowledged for the use of XPS and SEM instruments.

References

- [1] W.H. Hocking, F.W. Stanchell, E. McAlpine, D.H. Lister, Mechanisms of corrosion of Stellite-6 in lithiated high temperature water, *Corros. Sci.* 25 (1985) 531–557.
- [2] C. Maffiotte, M. Navas, M.L. Castano, A.M. Lancha, XPS characteristic of oxide films formed in cobalt-based alloys during corrosion tests at high temperature, *Surf. Interface Anal.* 30 (2000) 161–166.
- [3] W.H. Hocking, D.H. Lister, Corrosion of Stellite-6 in lithiated and borated high-temperature water, *Surf. Interface Anal.* 11 (1988) 45–59.
- [4] J.C. Wren, Steady-state radiolysis: effects of dissolved additives, in: Chien M. Wai, Bruce J. Mincher (Eds.), *Nuclear Energy and the Environment*, ACS Symposium Series 1046 American Chemical Society, Washington, DC, 2010, pp. 271–295.
- [5] J.M. Joseph, B.S. Choi, P. Yakabuskie, J.C. Wren, A combined experimental and model analysis on the effect of pH and O₂(aq) on gamma-radiolytically produced H₂ and H₂O₂, *Radiat. Phys. Chem.* 77 (2008) 1009–1020.
- [6] A. Foelske, H.-H. Strehblow, Structure and composition of electrochemically prepared oxide layers on Co in alkaline solutions studied by XPS, *Surf. Interface Anal.* 34 (2000) 125–129.
- [7] W. Feitknecht, W. Lotmar, ÜberMischfällungen von Nickel-Zink- und Kobalt-Zink-Hydroxyd (4. Mitteilung über topochemische Reaktionen kompakt-disperser Stoffe), *Helv. Chim. Acta* 18 (1935) 1369–1388.
- [8] M. Pontinha, S. Faty, M.G. Walls, M.G.S. Ferreira, M. Da Cunha Belo, Electronic structure of anodic oxide films formed on cobalt by cyclic voltammetry, *Corros. Sci.* 48 (2006) 2971–2986.
- [9] W.K. Behl, J.E. Toni, Anodic oxidation of cobalt in potassium hydroxide electrolytes, *Electroanal. Chem. Interfac. Electrochem.* 31 (1971) 63–75.
- [10] W.A. Badway, F.M. Al-Kharafi, J.R. Al-Ajmi, Electrochemical behaviour of cobalt in aqueous solutions of different pH, *J. Appl. Electrochem.* 30 (2000) 693–704.
- [11] T. Ohtsuka, N. Sato, Anodic oxide film on cobalt in weakly alkaline solution, *J. Electroanal. Chem.* 147 (1983) 167–179.
- [12] A. Gulino, G. Fiorito, I. Fragalá, Deposition of thin films of cobalt oxides by MOCVD, *J. Mater. Chem.* 13 (2003) 861–865.
- [13] M. Metikoš-Huković, R. Babić, Passivation and corrosion behaviours of cobalt and cobalt–chromium–molybdenum alloy, *Corros. Sci.* 49 (2007) 3570–3579.
- [14] T. Nishimura, H. Katayama, K. Noda, T. Kodama, Effect of Co and Ni on the corrosion behaviour of low alloy steels in wet/dry environment, *Corros. Sci.* 42 (2000) 1611–1612.
- [15] C.F. Baes, R.E. Mesmer, *The Hydrolysis of Cations*, second ed., Wiley, New York, 1986.
- [16] K. Daub, X. Zhang, J.J. Noël, J.C. Wren, Electrochemical study of iron oxide growth and conversion at temperatures between 25 and 100°C, *Electrochim. Acta* 56 (2011) 6661–6672.
- [17] M.C. Biesinger, B.P. Payne, A.P. Grosvenor, L.W.M. Lau, A.R. Gerson, Resolving surface chemical states in XPS analysis of first row transition metals, oxides and hydroxide: Cr, Mn, Fe, Co and Ni, *Appl. Surf. Sci.* 257 (2011) 2717–2730.
- [18] K. Daub, X. Zhang, J.J. Noël, J.C. Wren, Effects of gamma-radiation versus H₂O₂ on carbon steel corrosion, *Electrochim. Acta* 55 (2010) 2767–2771.
- [19] Q.W. Knapp, J.C. Wren, Film formation on Type-316L stainless steel as a function of potential: Probing the role of gamma-radiation, *Electrochim. Acta*, (submitted for publication).
- [20] K. Daub, X. Zhang, J.J. Noël, J.C. Wren, Gamma-radiation-induced corrosion of carbon steel in neutral and mildly basic water at 150 °C, *Corros. Sci.* 53 (2011) 11–16.
- [21] M. Pourbaix, *Atlas of Electrochemical Equilibria in Aqueous Solution*, New York, Oxford, 1966.
- [22] L.J. Oblonsky, T.M. Devine, A surface enhanced Raman spectroscopic study of the passive films formed in borate buffer on iron, nickel, chromium and stainless steel, *Corros. Sci.* 37 (1995) 17–41.
- [23] R. Cheng, B. Xu, C.N. Borca, A. Sokolov, C.S. Yang, L. Yuan, S.H. Liou, Characterization of the native Cr₂O₃ oxide surface of CrO₂, *Appl. Phys. Lett.* 79 (2001) 3122–3124.
- [24] U. Luders, F. Sanchezj, J. Fontcuberta, Initial stages in the growth of {111}-faceted CoCr₂O₄ clusters: mechanisms and strained nanometric pyramids, *Appl. Phys. A* 79 (2004) 93–97.
- [25] D. Marijan, M. Gojić, Electrochemical study of the chromium electrode behaviour in borate buffer solution, *J. Appl. Electrochem.* 32 (2002) 1341–1346.
- [26] G.J. Brug, A.L.G. van den Eeden, M. Sluyters-Rehbach, J.H. Sluyters, The analysis of electrode impedances complicated by the presence of a constant phase element, *J. Electroanal. Chem.* 176 (1984) 275–295.
- [27] A.P. Grosvenor, B.A. Kobe, M.C. Biesinger, N.S. McIntyre, X-ray photoelectron spectroscopy studies of chromium compounds, *Surf. Interface Anal.* 36 (2004) 1550–1563.
- [28] G.T. Burstein, A.J. Davenport, The current-time relationship during anodic oxide film growth under high electric field, *J. Electrochem. Soc.* 136 (1989) 936–941.